Particle image velocimetry measurement of the velocity field in turbulent thermal convection

Ke-Qing Xia,* Chao Sun, and Sheng-Qi Zhou†
Department of Physics, The Chinese University of Hong Kong, Shatin, Hong Kong, China
(Received 1 August 2003; published 17 December 2003)

The spatial structure of the velocity field in turbulent Rayleigh-Bénard convection in water has been measured using the particle image velocimetry technique, with the Rayleigh number Ra varying from 9×10^8 to 9×10^{11} and the Prandtl number remaining approximately constant (Pr$\simeq$4). The study provides a direct confirmation that a rotatory mean wind indeed persists for the highest value of Ra reached in the experiment. The measurement reveals that the mean flow in the central region of the convection cell is of the shape of a coherent elliptical rotating core for Ra below 1×10^{10}. Above this Ra, the orientation of the elliptical core changes by a 90° angle and an inner core rotating at a lower rate inside the original bulk core emerges. It is further found that the rotation frequencies of the inner core and the outer shell have distinct scalings with Ra; the scaling exponent for the outer-shell is 0.5 and it is 0.4 for the inner core. From the measured rms and skewness distributions of the velocity field, we find that velocity fluctuations at the cell center are neither homogenous nor isotropic. The turbulent energy production fields further reveal that the mean wind is not driven by turbulent fluctuations associated with Reynolds stress.

DOI: 10.1103/PhysRevE.68.066303 PACS number(s): 47.27.Nz, 44.25.+f, 47.32.−y

I. INTRODUCTION

Fluid turbulence often exhibits complex and seemingly random behavior but at the same time, depending on the time and length scales one looks at, it is capable of organizing itself into highly coherent and symmetric structures. The Rayleigh-Bénard convection is a good system to demonstrate this. Convective thermal turbulence is interesting. Not only does it have obvious engineering applications and but it also is an ideal model for studying turbulence in a closed system. A full understanding of convective turbulent flow in this ''simple'' system will thus shed light on a range of more complicated convection problems occurring in nature, such as those in the planets, the oceans, and the atmosphere. The current work attempts to address the following three issues: (1) The structures, statistics, and dynamics of the global velocity field; (2) the persistence of the mean wind at very high Rayleigh numbers; and (3) the scaling of the wind velocity with the Rayleigh number Ra.

A. Structures and dynamics of the global velocity field

A distinct feature of turbulent thermal convection in a closed box is a large-scale circulatory flow (LSC), also referred to as the ''wind'' in turbulent convection. This wind was observed by Krishnamurti and Howard through flow visualization studies [1]. Since then there have been extensive studies of this large-scale mean flow through both semiquantitative techniques and quantitative measurements. For a brief summary of some of the earlier results, we refer the reader to the papers by Grossmann and Lohse [2] and Chavanne *et al.* [3]. The recent paper by Qiu and Tong also contains a review of various velocity measurements and techniques in turbulent convection [4]. Through these measurements we now have a good idea about the spatial structure and the scaling with the Rayleigh number Ra and the Prandtl number Pr of the mean wind. On the other hand, the limitations of the various techniques have prevented us from obtaining a precise picture on the global velocity field. This is partly because most of the quantitative studies of the velocity field are confined to local measurements either at a single point or at scans along certain symmetry axes of the convection box [3,4], which, as we will see later in this paper, can miss some of the important features in the flow field. To our knowledge, some of the fundamental quantities important for understanding the dynamics that drives turbulent flow have not been measured quantitatively so far. These include the Reynolds shear stress and turbulence production.

B. Persistence of the mean wind at very high Rayleigh numbers

A natural question one may ask is ''what will happen to the fluid's large-scale coherent rotatory motion at very high values of Ra?'' In other words, is the wind the asymptotic flow structure in the convection box? There is evidence that the wind may have reached a ''stable'' or ''asymptotic'' state for Ra larger than 1×10^{11}, in the sense that the flow is in a more symmetric configuration with respect to the directional reversal of the wind [5]. But so far most of the studies of the spatial structure of the velocity field that directly confirm the existence of a circulatory wind are made for Ra$\sim10^9$; these include flow visualizations [6] and systematic laser-Doppler velocimetry measurements [4]. Note that many local velocity measurements, i.e., at a point off the sidewall, in systems such as helium gas have been made with Ra reaching $\sim10^{13}$ and some of the results may be taken to be consistent with the wind picture [5,7], but they nevertheless do not provide a direct confirmation of it. As Sreenivasan, Bershdskii, and Niemela argued recently, for Pr close to that of water a value of Ra around 10^{12} is needed for the boundary layer to be

*Email address: kxia@phy.cuhk.edu.hk
†Present address: Department of Physics and iQUEST, University of California, Santa Barbara, CA 93106, USA.

fully turbulent and therefore the flow field to be regarded as developed turbulence [8]. Thus, a whole-field velocity measurement reaching this level of Ra becomes an interesting test for the wind picture.

C. Scaling of the wind velocity

One of the standing issues in turbulent Rayleigh-Bénard convection concerns the precise value of the scaling exponent γ of the mean wind with Ra (i.e., $V \sim \mathrm{Ra}^{\gamma}$), for which γ ranging from 0.4 to 0.5 has been reported in the literature [3,9–11]. These can be largely classified into two categories. One measures the absolute magnitude of the wind and most results in this group yield $\gamma \approx 0.5$. The other measures the oscillation frequency of the wind and γ from this group ranges from 0.42–0.47. As we will see below, this discrepancy comes partly from the fact that different experiments measuring velocity at different places or making different ''regional averages'' in the convection cell. The fact that different techniques may have different measurement bias may also contribute to the differences.

D. The present work and organization of the paper

In this paper we report a direct measurement of the global velocity field in turbulent Rayleigh-Bénard convection using the particle image velocimetry (PIV) technique. The main advantage of the PIV method is its ability to make instantaneous velocity measurements for the whole flow field [12]. But even for measuring time-averaged flow properties, PIV's ability for making simultaneous whole-field measurements greatly reduces the time required for determining the spatial structures of the velocity field. Our experiments are conducted in water and the range of Ra varied from 9×10^{8} to 9×10^{11} while the Prandtl number Pr remained approximately constant (~ 4). In addition to the mean velocity field, some statistical quantities, such as the rms and skewness of the velocity field, and turbulent kinetic and Reynolds shear stress fields are also measured for selected values of Ra. The measurement reveals detailed structures and properties of the flow field, and yields a precise value of the scaling exponent for the rotational frequency of the wind over three decades of Ra in a single experiment. In addition, we find a hitherto unreported transition in the flow state. The time-averaged convective flow in the central region of the convection cell forms a coherent rotatory core, as was found previously [13]. However, for Ra above 1×10^{10} we find this rotatory core separates into an inner-core and an outer shell, which rotate at different frequencies and have different scaling exponents with Ra.

The remaining part of this paper is organized as follows. Section II contains descriptions about the construction of the convection cells used in the experiment, details of the PIV measurements, and the experimental parameters. In Sec. III we present and discuss the experimental results, which are divided into four parts: III A, mean velocity field; III B, statistical quantities; III C, instant velocity field, and III D, velocity in the plane perpendicular to the wind. In Sec. IV we summarize our findings and present the conclusions.

II. EXPERIMENT

A. The convection cells

The choice for the shape of the convection box is based on the following considerations. For the most widely used cylindrical shape, the curved sidewall will introduce distortions in the images viewed by the camera. Although this distortion can be partly corrected by fitting a square-shaped jacket outside the convection cell, the jacket unavoidably limits the field of view in regions near the top and bottom plates. For a cube-shaped cell, it is known that the mean flow is confined in the diagonal plane of the box [6,14], which means that the PIV method will measure only a projection of the flow field. With these in mind, a rectangular shape is chosen for the convection box. To extend the varying range of the Rayleigh number, two convection cells are used in the experiment. The length, width, and height of the ''small cell'' are $25\times7\times24$ (cm) and those of the ''large cell'' are $81\times20\times81$ (cm). With this geometry, the large-scale flow is expected to be largely confined in the plane with the aspect ratio $\Gamma \approx 1$ and the PIV measurement of velocity in this plane will capture the dominant features of the flow.

The small cell is made of Plexiglas sidewall with gold-plated copper as the top and bottom conducting plates, with the plates' temperatures monitored by four embedded thermistors, two in each one. Other features of the cell are similar to those of a cubic cell with a dimension of 25 cm on the side, which has been previously described in detail elsewhere [14,15]. Figure 1 shows a schematic drawing of the large convection cell: (a) front view and (b) cross-section view. The top and bottom conducting plates, indicated as *A* and *B* in the figure, are made of pure copper of thickness 3 cm and their surfaces are electroplated with nickel and then chromium. The reason for the double coating is that nickel has a good bonding with copper and chromium provides protection against oxidation by water. A stainless steel cover (C) is attached on the top of the upper plate; this cover together with the upper surface of the top copper plate served as a cooling chamber to exchange heat with a circulating chiller (N8 KT-50W, Thermo Haake Co. Maximum cooling power 5000 watts). The design of the cooling chamber is inspired by the design of the mercury convection cell by Glazier *et al.* [16]. The chamber is divided into two compartments by a stainless steel plate, wielded on the plate are 60 tubes each of 5 mm in diameter and pointing vertically downward [see Fig. 1(b)]; the tubes are distributed uniformly over the plate. Cooling water is first pumped into the upper compartment through eight inlet nozzles (D), four on the front and four on the back, as shown in the figure. The tube diameter and circulator flow rate are such that the incoming cooling water will first fill the upper compartment, then flow to the lower one through the 60 tubes, impinge on the copper plate, and cool it directly. Finally, the cooling water exits the chamber through the eight outlet nozzles in the lower compartment (three on the front, three on the back, and one each on the left and right side). Such design ensures the temperature uniformity over the plate and provides a high flow rate for efficient thermal exchange. Eight aluminum strip heaters (E) of size 102×203 mm (Tempco Electric Heater Corp.), which

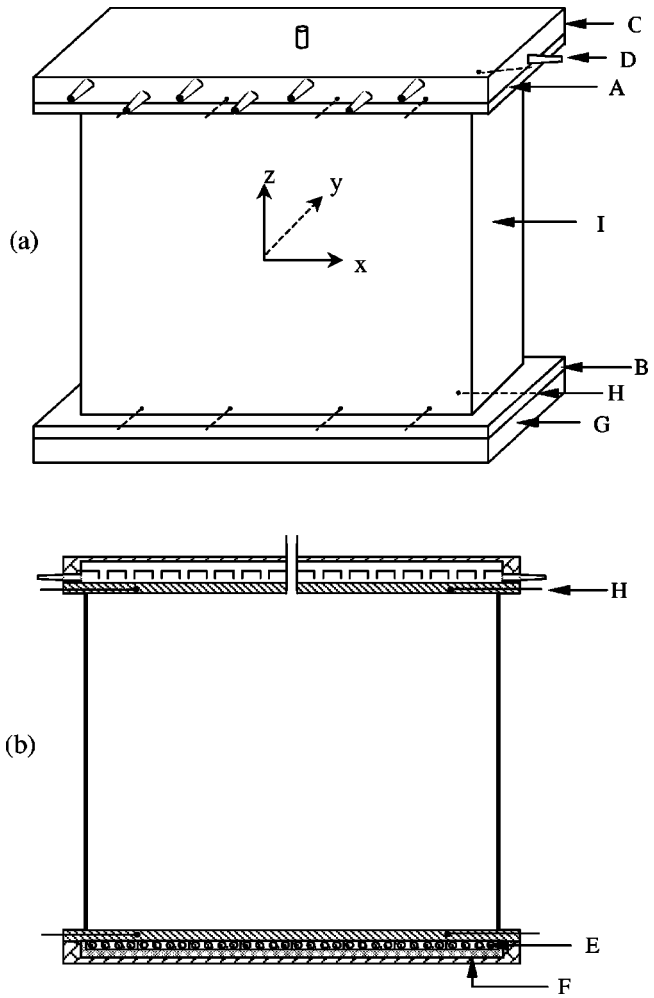

FIG. 1. Schematic drawing of the large convection cell and the coordinates of the experiment: (a) front view; (b) cross-section view of the middle vertical plane. *A* and *B* are the top and bottom copper plates, respectively. *C*: cooling chamber; *D*: inlet and outlet nozzles; *E*: heaters; *F*: insulating plate; *G*: stainless steel bottom cover; *H*: thermistors; and *I*: sidewall box.

are specially designed for efficient heating of flat surfaces, are arrayed beneath the lower plate. A heat transfer compound was spread over the surface and the sides of the heaters before they were attached to the bottom plate to ensure good thermal contact between the plate and the heaters and among the heaters themselves. An insulating plate (F) was inserted between heaters and the stainless steel bottom cover *G*. The heaters are powered by a dc power supply with 5000 watts of maximum power (DCR 300-16T, Sorensen Co.). Twenty thermistors *H* (2.4 mm diameter in size, model No. 44031, Omega Engineering Inc.) were embedded inside the copper plates beneath the conducting surfaces, ten in each one. These thermistors serve to monitor the temperature uniformity across each plate and are also used to measure the temperature difference ΔT across the cell. The sidewalls (I) are made of 2 cm thick Plexiglas plates glued together to form a rectangular box. A groove is machined on the surface of the conducting plates and an o-ring is placed inside for water-tight sealing between the plates and the sidewall box. The top and bottom plates and the sidewall are then held together by stainless steel posts (not shown). The top and bottom part of the cell are wrapped with nitrile rubber sheets for thermal insulation. With this setup, the cell's conducting plates have temperature stability and uniformity better than 1% of the temperature difference across the cell.

B. The PIV measurement

As shown in Fig. 1, the Cartesian coordinate for the experiment is defined such that its origin coincides with the cell center, its x axis points to the right, the z axis points upward, and the y axis points inward. As already mentioned, given the geometry of both cells the LSC is expected to be confined mainly within the xz plane, where the relevant aspect ratio for the flow is unity and where most of the PIV measurement are made in this experiment. The PIV system consists of a dual Nd:YAG (yttrium aluminum garnet) laser operated at an energy of 80 mJ per pulse, a lightsheet optics, a cooled charge-coupled device (CCD) camera (12 bit dynamic range and 1.3K$\times$1K-pixel spatial resolution), a synchronizer, and a PIV control and analysis software (TSI, Inc.). The seeding particles used in the experiment are 50 μm diameter polyamid (density$=1.03$ g/cm^3) spheres [17]. A two-dimensional (2D) velocity map is obtained by cross-correlating two consecutive images separated by a time interval ranging from 20 to 100 ms which is selected optimally according to the flow speed. Each 2D velocity vector is calculated from a subwindow (32×32 pixels) that has 50% overlap with its neighboring subwindows [18]. For the small cell, the entire flow field comprises 60×60 velocity vectors measured all at once. For the large cell, the 2D field is divided into quarters and they are measured one at a time. The time-averaged flow field is then a composite of four quarters consisting of 120×120 velocity vectors. For most values of Ra the sampling rate is 0.25 Hz, and each measurement averages over 3000 and 1280 instant vector fields for the small and the large cells, respectively. For two Ra values (3.8×10^9 and 3.5×10^{10}, in small cell), the average is over 15 000 vector maps at a sampling rate of 3 Hz so that certain statistical quantities of the velocity field are obtained. Also for these two values of Ra, measurements are made in the yz plane at $x=0$, i.e., in the plane perpendicular to the large-scale flow, so that a more complete picture of the flow field is obtained.

C. The experimental conditions

Water is used as the convecting fluid. The control parameter in the experiment is the Rayleigh number Ra $=\alpha g L^3 \Delta T/\nu\kappa$, with g being the gravitational acceleration, L the height of the cell, and α, ν, and κ being, respectively, the thermal expansion coefficient, the kinematic viscosity, and the thermal diffusivity of water. To prevent temperature drift and maintain constancy of the Prandtl number Pr$(=\nu/\kappa)$ for different values of Ra, two thermostats with temperature stability better than 0.1 °C and with windows for PIV measurements are built to house the cells. In the experiment, Ra varied from 9×10^8 to 3.5×10^{10} in the small cell and from 2×10^{10} to 9×10^{11} in the large cell, and Pr ($\simeq4.3$) remains approximately constant. During the experi-

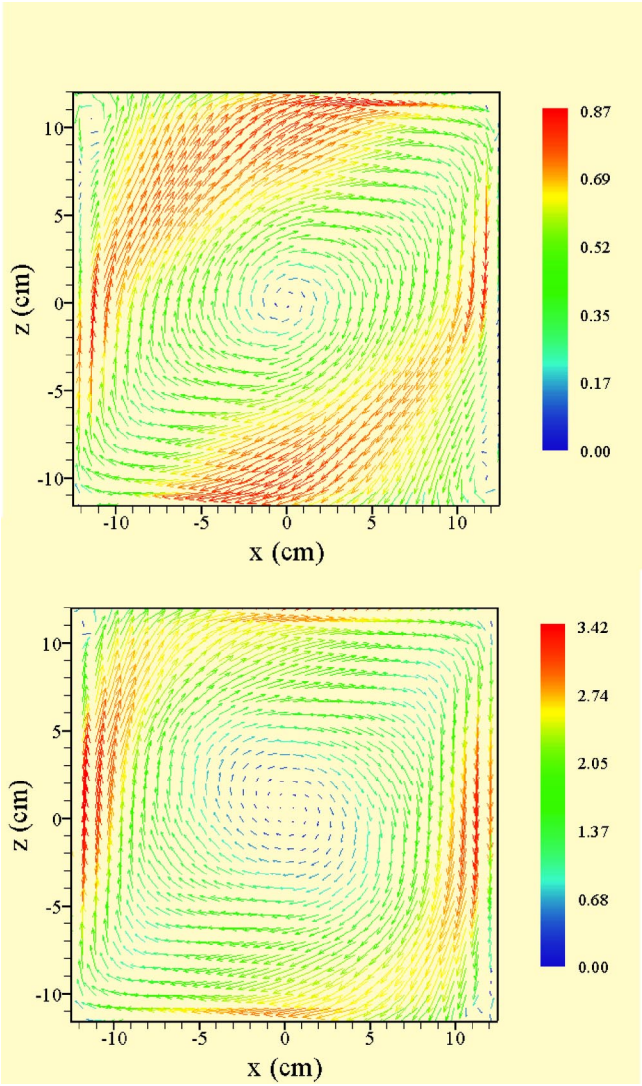

FIG. 2. (Color online) Coarse-grained vector maps of the mean velocity field with the magnitude $\sqrt{U^2+W^2}$ coded in both color and the size of the arrow in units of cm/s for Ra$=3.8\times10^9$ (top) and 3.5×10^{10} (bottom).

ment, the bottom plate of the cell is heated with constant power so that it is under a constant-flux boundary condition, but at steady state its temperature remains effectively constant; the top plate's temperature is regulated so that it is under constant-temperature boundary condition.

III. RESULTS AND DISCUSSION

A. Time-averaged velocity field

We first look at the gross features of the mean flow field by examining the ''coarse-grained'' two-dimensional vector map. Figure 2 shows two examples, for Ra$=3.8\times10^9$ (top) and 3.5×10^{10} (bottom), which are obtained by combining every two neighboring vectors into one, thus the spatial resolution is halved. In the figure the magnitude of the mean velocity $(U^2+W^2)^{1/2}$ is coded by color and by the length of the arrow, where $U=\langle u(t)\rangle$ and $W=\langle w(t)\rangle$ are the time-averaged x and z components of the velocity, respectively. The figure shows clearly that the mean flow is a clockwise rotatory motion and, as Ra increases, the high velocity regions are becoming increasingly concentrated along the perimeter of the cell with a relatively quiet central region. A closer inspection of the figure shows that the orientation of the central region is different for the two Rayleigh numbers. This becomes evident in the full-resolution (non-coarse-grained) color-coded contour maps shown in Fig. 3 for four values of Ra, where three lower values of Ra are from the small cell, and the highest Ra is from the large cell and hence is a composite of four separate measurements. Note that the contour map for the highest Ra does not fully cover the extent of the cell in the xz plane. Because of the strong reflections of light from the wall and the plates in this cell, the regions about 2 cm from the cell boundaries become inaccessible to the measurement [19]. For the small cell, the measurement can access essentially the entire 2D plane except regions very close to the cell boundaries ($\sim$ a few mm). By looking at the contour maps, one can immediately identify four features or regions of the flow field: (1) a central low-velocity elliptical core; (2) two low-velocity or stagnation regions represented by the blue spots at the lower-left and upper-right corners; (3) two high-velocity regions represented by the ''reddish bands,'' one stretches from the eight-o'clock position to the one-o'clock position and the other from the two-o'clock position to the seven-o'clock position; and (4) two counterrotating vortices at the upper-left and lower-right corners [20]. We shall discuss these features in turn.

That the flow field in the central region of the convection cell has an elliptical shape (at least for aspect ratio one cell) has been suggested previously. Based on the shadowgraphic study of the motions of thermal plumes by Zocchi, Moses, and Libchaber [6], Kadanoff drew a highly suggestive cartoon that implies the mean flow in the cell takes an elliptic shape [21]. A more quantitative evidence comes from Qiu and Tong, who proposed, based on their LDV measurement of mean velocity profiles, that the mean flow is of an elliptic shape rather than a circle [4]. The present study now provides the direct evidence that the central region is indeed of an elliptical shape. Figure 3 also indicates that the large-scale flow becomes increasingly concentrated near the perimeter of the cell with increasing Ra. This becomes more evident if we look separately at the contour maps for the horizontal and vertical components of the velocity field as shown in Fig. 4, where positive is defined as upward and rightward going for $W(x,z)$ and $U(x,z)$, respectively. By measuring the change of the flow's effective path-length with Ra, Niemela and Sreenivasan recently suggested that the mean flow will change its shape from ellipselike to squashlike as Ra increases [22]. Now the PIV result provides direct evidence for this. Figure 3 also clearly shows that the central elliptical core changes its orientation above Ra $\sim1\times10^{10}$, which as we will see below is associated with the emergence of an inner core inside the rotatory bulk central core (note that the low velocity bluish region in all the four images of Fig. 3 has an even darker bluish region inside it; this is an artifact of the color-coding scheme and is not the inner-core referred to here, which is defined by the shape of the velocity profiles).

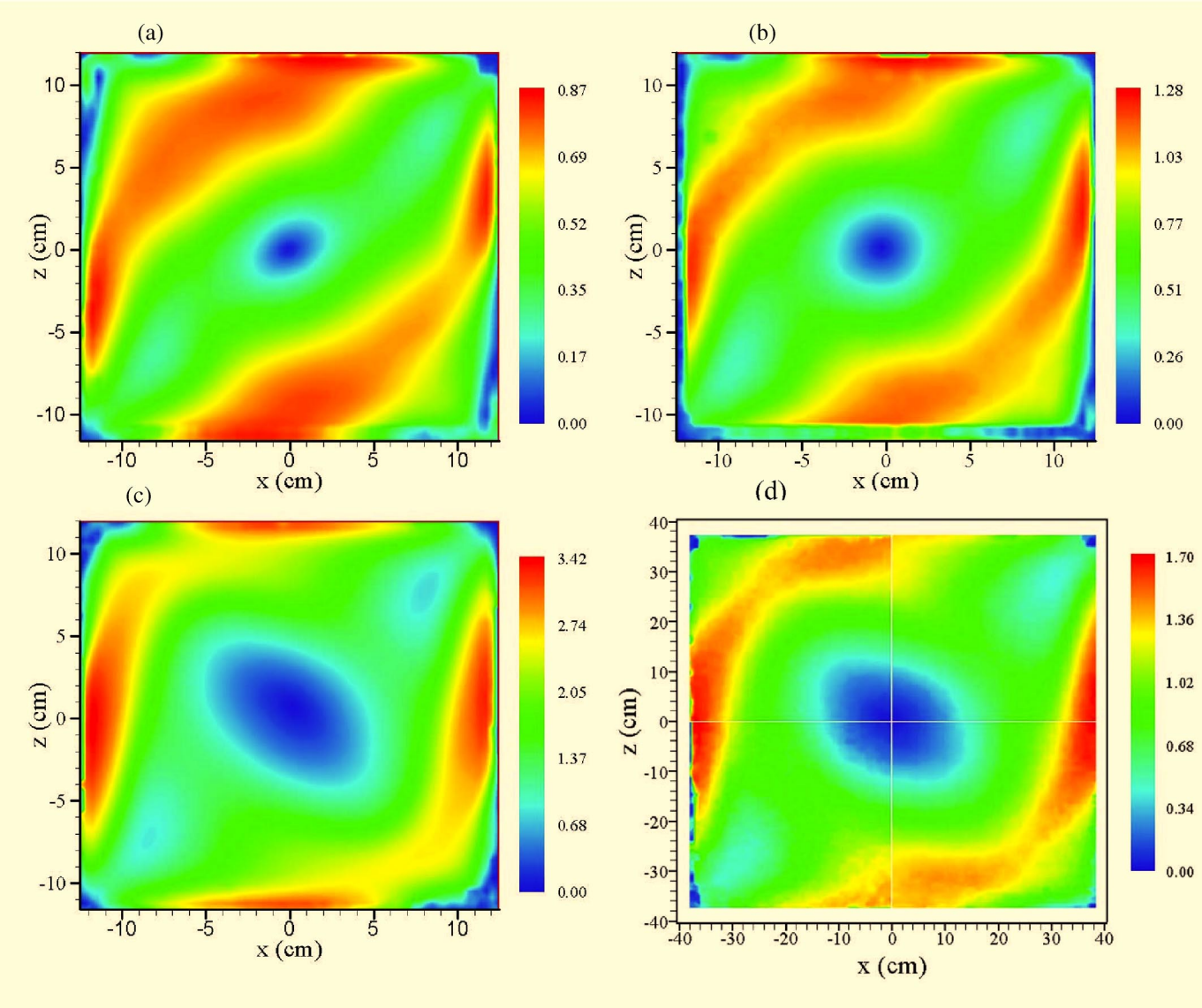

FIG. 3. (Color online) Color-coded contour maps of $\sqrt{U^2+W^2}$ for four values of Ra: (a) 3.8×10^9, (b) 7.5×10^9, (c) 3.5×10^{10}, and (d) 1.1×10^{11}.

To understand the dynamics that drives the mean wind and the evolution of the wind towards the cell's perimeters, we also made visualization studies of the motions of thermal plumes using thermochromic liquid crystal particles. These studies show that the thermal plumes that are generated from the conducting plates are swept to the low-velocity blue spots at the corners by the horizontal wind and then ''turn'' vertically to start their ascending/decending motions. As we will see below, this turning produces large Reynolds shear stress. It appears to us that, at least some of the time, an accumulation and/or a combination of plumes occur in these stagnation regions, which is manifested by the phenomenon that the plumes sometimes are going up/down in groups or clusters. Because the larger size will slow down the ''heat loss'' of plumes through thermal diffusion, this will allow the plumes to generate a more buoyant driving force as they rise/fall. Qiu and Tong have also argued previously that plumes need to combine to form ''composite'' plumes in order to have a long-enough lifetime to cross the cell [23]. We note that even if the plumes do not form composite ones, by traveling in groups they will reduce their effective heat loss to the surrounding fluid. If the plumes indeed accumulate or ''wait'' in the stagnation regions (to gather enough ''critical mass'' or buoyancy or some triggering instability) before starting their vertical motions, it will mean the motion of the mean wind is not really ''continuous'' but is made up of a two-leg ''relay race,'' which corresponds to the two red bands and is performed by the hot and cold plumes, respectively (the flow is of course continuous due to mass conservation). Similar views have been advanced by Villermaux theoretically [24] and by Qiu and Tong based on their study of the correlated temperature signals from the opposite sidewalls [4,23]. In this picture, in steady state convective flow the release of the ''plume clusters'' from the two stagnation regions becomes coordinated in time in a quasiperiodic fashion so the relay race is well synchronized. This is consistent

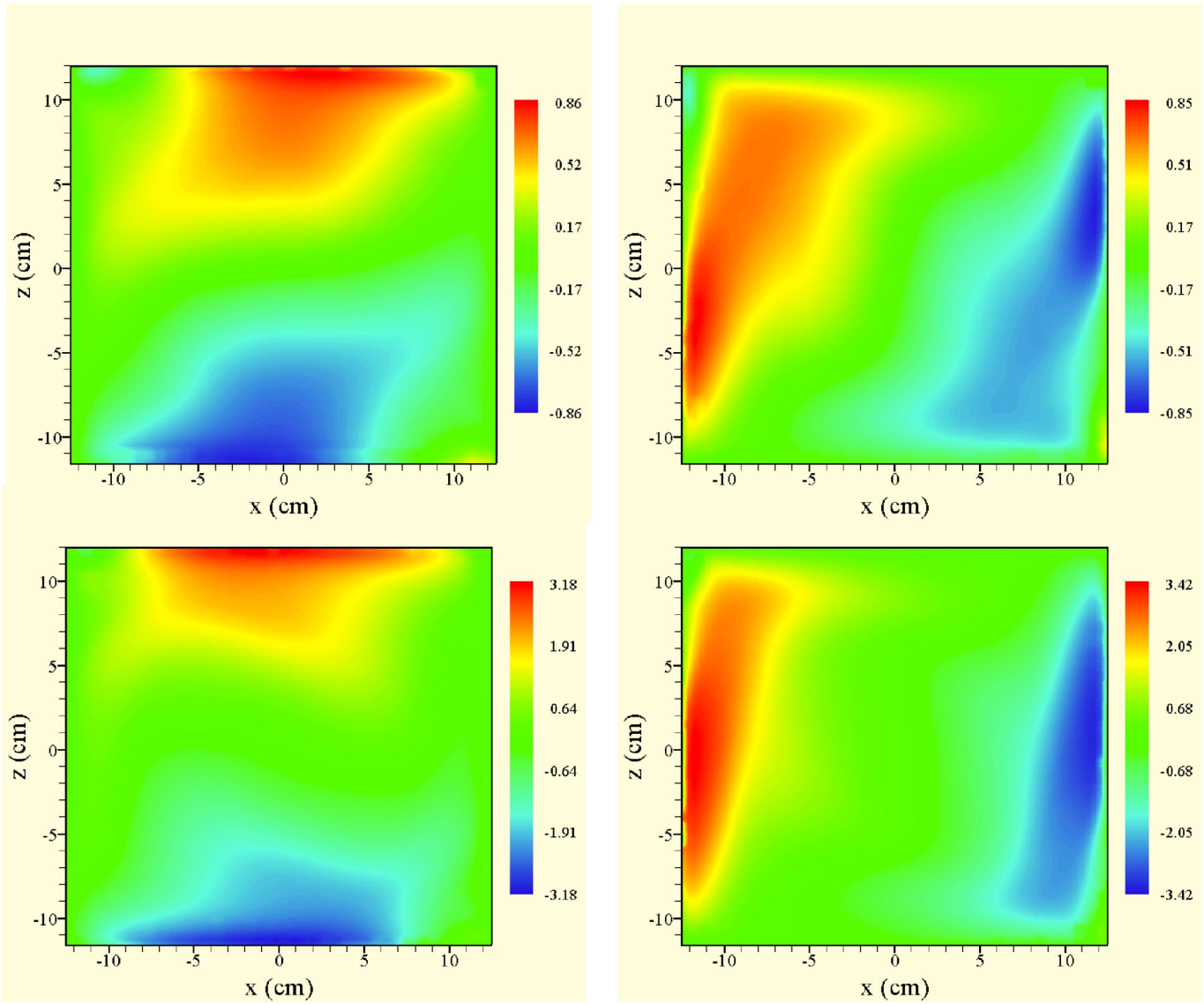

FIG. 4. (Color online) Contour map plots of the horizontal (left panel) and vertical (right panel) components of the mean velocity, for $\mathrm{Ra}=3.8\times10^{9}$ (upper panel) and 3.5×10^{10} (lower panel). Positive is defined for upward and leftward motions and color coding is in cm/s.

with the recently measured result for the instantaneous heat flux near the sidewall which shows intermittent or quasiperiodic behavior [25], since heat is predominantly transported by plumes.

As the rising and falling plumes accelerate along the sidewalls they create the regions of high mean velocity or the reddish bands, the one from eight-o'clock to one-o'clock positions is due to the rising hot plumes and the other falling cold plumes. These plume-motion dominated regions are also the regions that contain most of the kinetic energy of the flow field as is shown in Fig. 5, where the color-coded mean kinetic energy per unit mass in the xz plane $K=(U^2+W^2)/2$, in units of $(\mathrm{cm/s})^2$, is shown for $\mathrm{Ra}=3.8\times10^{9}$ (top) and 3.5×10^{10} (bottom). As Ra increases the plumes become more energetic and are more able to "shoot" straight, resulting in the high velocity regions to become increasingly confined near the perimeter of the cell and the growth of the central low-velocity bluish region. This result provides direct evidence to the intuitive physical picture that thermal plumes rising and descending along opposite sidewalls are responsible for driving the rotational bulk flow (or "flywheel") in the convection cell [9,21].

Since the large-scale flow is mainly confined near the perimeter of the cell, it would be useful to examine the velocity field near that region. Figure 6(a) shows the variations from the lower plate to the top plate of the horizontal $U(z)$ and vertical $W(z)$ velocity components "cut" at a distance 2 cm from the left sidewall (small cell). Figure 6(b) shows the profiles of $U(x)$ and $W(x)$ cut at a distance 2 cm below the top plate, for $\mathrm{Ra}=3.8\times10^{9}$. Keep in mind that near the sidewalls the vertical velocity W is the dominant velocity component and the same role is played by the horizontal velocity U near the plates. If we combine W and U profiles near the sidewall and the plate, we can have an approximate picture on how a fluid parcel (or a thermal plume) accelerates and decelerates as it rises from the lower-left corner to the top

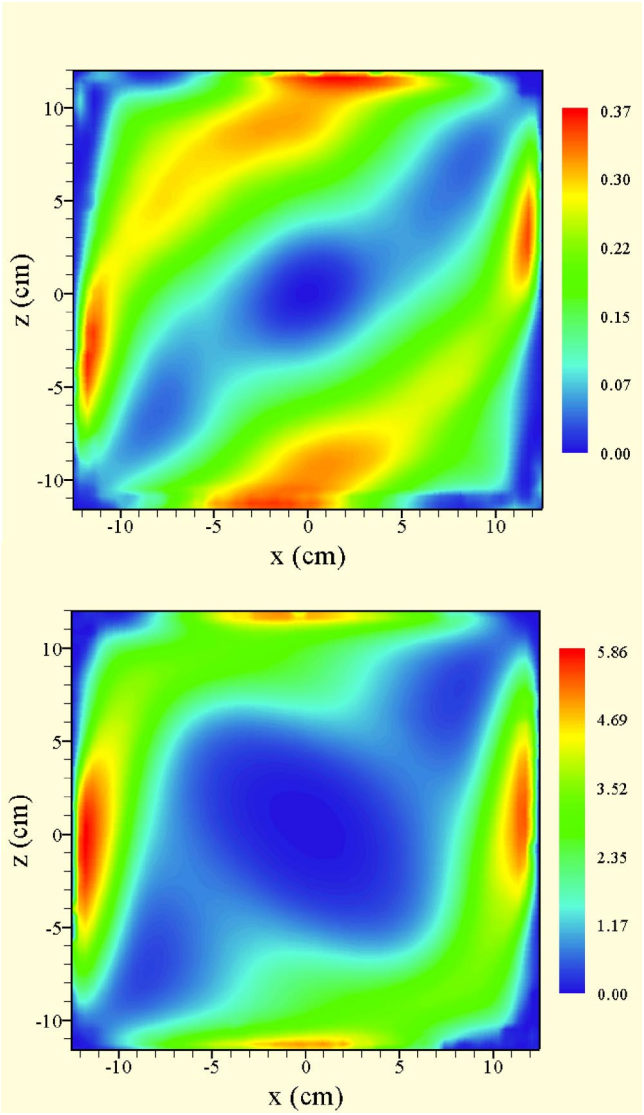

FIG. 5. (Color online) Distribution of the mean flow kinetic energy per unit mass $(U^2+W^2)/2$ in units of $(\mathrm{cm/s})^2$ for $\mathrm{Ra}=3.8\times10^9$ (upper panel) and 3.5×10^{10} (lower panel).

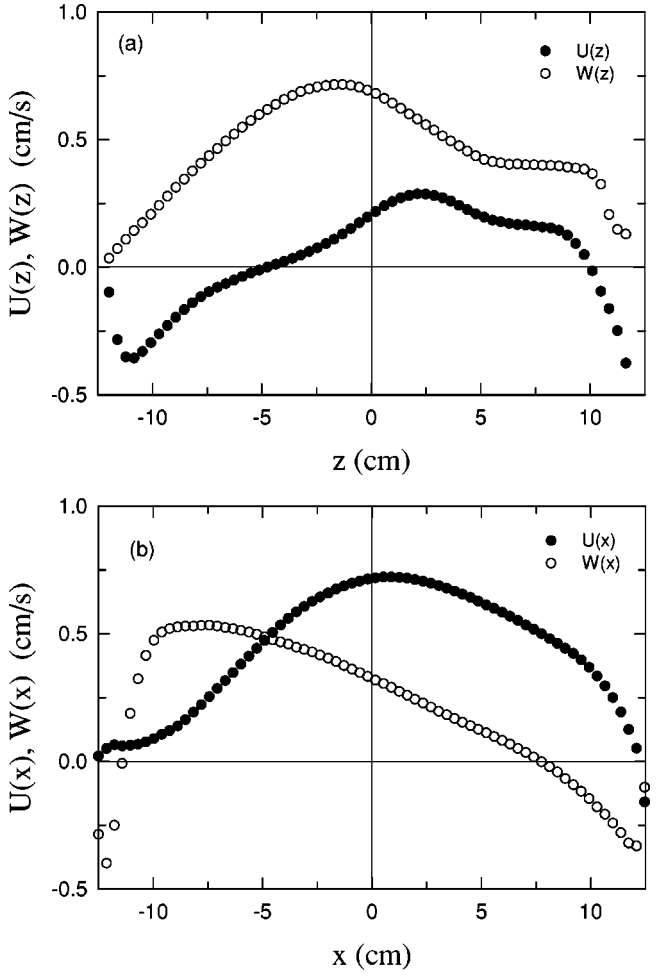

FIG. 6. Profiles of the horizontal velocity U and vertical velocity W cut, respectively, at (a) 2 cm from the sidewall and (b) 2 cm below the top plate (b), for $\mathrm{Ra}=3.8\times10^9$.

plate and then move to the top-right corner. The sign changes of the ''minor'' component also tell us how the flow changes directions near the corner. Note that the large negative values of $U(z)$ near the top plate corresponds to the small vortex rotating counterclockwise at the top-left corner as seen in Figs. 2 and 3. Counterrotating vortices at cell corners have been seen previously by Tilgner, Belmonte, and Libchaber in a cubic cell [26]. Another feature shown in Fig. 6 is that the maximum values of dominant components (W near sidewall and U near the plate) are not at the positions of the ''symmetry axes'' (the x and z axes in this case), which means that ''scans'' along these axes in local velocity measurements do not measure the maximum value of the velocity field.

To study quantitatively the overall rotational motion of the central bulk region, we examine the mean velocity profiles cut along the symmetry axes of the cell. The left panel of Fig. 7 shows the ''vertical cut'' (at $x=0$) of the horizontal velocity component U and the right panel shows the ''horizontal cut'' (at $z=0$) of the vertical component W for three values of Ra as indicated on the figure. The first thing we would like to note is that the profiles do not reveal the detailed structure in the boundary layer region, since our PIV measures the flow field in the entire xz plane and is not focused on the boundary layer region. Thus the profiles in Fig. 7 do not show that the velocity decays to zero near the wall and plates as it should. Tilgner, Belmonte, and Libchaber have previously measured the profile $U(z)$ in a cubic cell [26], and their profile shows more details in the boundary layer region and is able to resolve the boundary layer thickness. On the other hand, their profile does not show the ''hump'' (or ''dip'') seen in our profile (around $z\approx9$ cm for the small cell). This hump was also not observed in velocity profiles measured in cylindrical cells [4]. Because we see the same feature from LDV-measured profiles in the same cell [27], we know this hump is not an artifact of the PIV measurement. Since the mean flow in the cubic cell is along the diagonal direction, it is not necessary that its flow structure be the same as ours. Another reason that Tilgner, Belmonte, and Libchaber did not see the hump in their profile could be due to the limited spatial resolution of their measurement, as they used an electrochemical labeling technique that requires the manual accumulation of data [26].

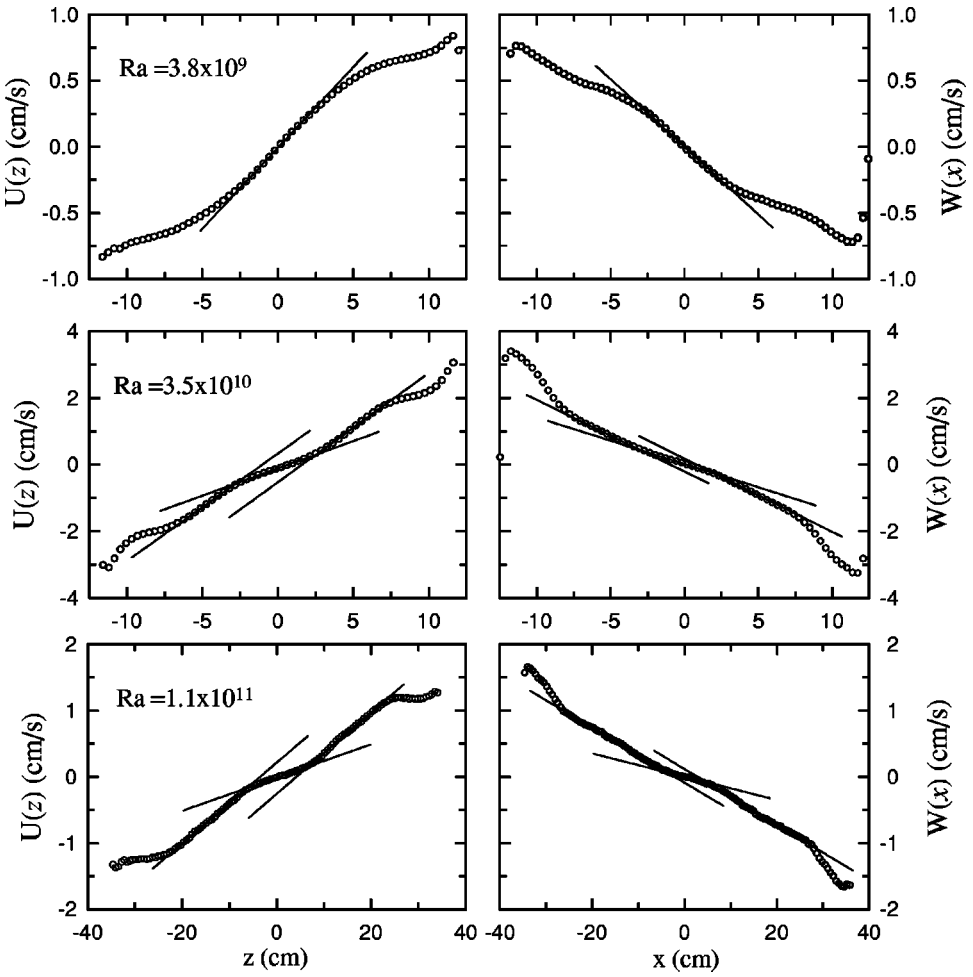

FIG. 7. Left panel: Horizontal velocity profiles $U(z)$ cut along the z axis (at $x=0$) for three values of Ra as indicated. Right panel: Vertical velocity profiles $W(x)$ cut along the x axis (at $z=0$) for the same Ra values.

A striking feature of the profiles shown in Fig. 7 is the qualitative change in shape with Ra. At lower Ra the velocity in the central part of the convection cell is a linear function of the distance from the cell center, indicating the existence of a central core that rotates about the y axis of the cell. A rigid-body-like coherent rotatory central core in turbulent convection was first observed by Qiu, Yao, and Tong [13] in a cylindrical cell. For the two higher values of Ra, however, the central linear part of the profile changes into three-segment lines with the two outer ones having the same slope which is larger than that of the central one. This indicates that with increasing Ra the innermost region of the central core appears to be unable to follow the motion of the outer region (which is ''driven directly'' by plumes) and an inner-core rotating at a slower rate emerges for $\mathrm{Ra}\gtrsim 1\times 10^{10}$. It is found that the size of the inner-core remains approximately constant $[\sim(0.15-0.2)L]$ as Ra increases up to 9×10^{11}. Figure 7 also shows that the velocity profile of the inner-core goes through the cell center, indicating it is the center of rotation for the inner core. On the other hand, the profile for the outer shell does not go through the cell's center. In fact, if we take a point in the inner core and a point in outer shell and calculate the ratio $(v_o-v_i)/(r_o-r_i)$, we find that this ratio is approximately constant for any pair of points, indicating the center of rotation for the outer shell is not fixed but moving along the circumference of the inner core. In the above, v and r are the velocity of and radial distance from the cell center for the outer-shell point o and inner-core point i, respectively. To our knowledge, the existence of an inner rotation core inside an outer one in turbulent Rayleigh-Bénard convection has not been reported previously, nor is there a theoretical prediction for it. Because the rotatory motion of the bulk fluid is driven by the rising and falling thermal plumes along the sidewalls, one may expect that the driving force will weaken towards the interior of the cell. But this would be expected to occur in a continuous fashion, not a sharp change as manifested in Fig. 7. Note that the time-averaged temperature in the bulk of the convection cell is essentially homogeneous, which means the viscosity of the convecting fluid in the core and the shell should be the same. Thus there is a large mismatch of viscous shear stress at the inner-outer core boundary. The questions now are why this sharp change in the shear rate and what determines the position of the core-shell boundary?

The slope of the linear part of the profiles provides the rotational frequency ω (or shear rate) of the corresponding core or shell. In addition to the cuts along the x and z axes, cuts along other directions such as the diagonal all show the same qualitative features. While the values of ω are slightly different for cuts along different directions, their Ra-scaling exponents are essentially the same. The small difference for

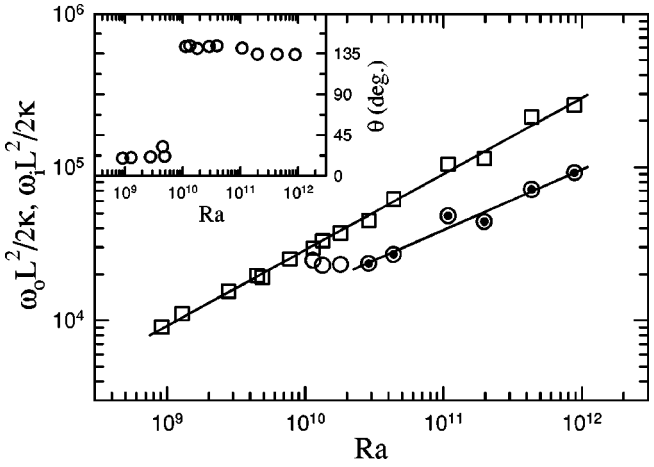

FIG. 8. Ra dependence of the normalized rotation rates $\omega L^2/2\kappa$ of the inner core (circles) and out shell (squares). The solid lines are power-law fits to the respective data. Inset: Orientation angle between the elliptical core and the horizontal.

frequencies from different cuts could come from the fact that our cell in the xz plane is not a perfect square, i.e., the aspect ratio is not exactly one, which introduces a symmetry breaking for the spatial structure in this plane. Clearly, more systematic investigation is needed to ascertain this. Figure 8 plots the normalized rotation frequency $\omega L^2/2\kappa$ vs Ra for the outer shell (squares) and inner-core (circles), respectively, where ω_o and ω_i are the average frequencies from the vertical and horizontal cuts of the shell and the core, respectively. The solid lines are power-law fits to the corresponding data: $\omega_o L^2/2\kappa = 0.318\mathrm{Ra}^{0.496}$ and $\omega_i L^2/2\kappa = 1.780\mathrm{Ra}^{0.395}$ (only for those points that appear to be beyond the ''transitional'' region, denoted by dotted circles). The inset plots the angle θ between the x axis and the major axis of the elliptical core, which shows that the emergence of the inner core around $\mathrm{Ra} = 1\times10^{10}$ corresponds to the flipping of the orientation of the outer shell. Note that for lower Ra the core is not along the diagonal of the cell ($\theta \simeq 20°$), whereas after the transition the elliptical core is aligned along the other diagonal of the cell ($\theta \simeq 135°$). This higher symmetry suggests that the flow structure is in a more stable state for Ra $\gtrsim 1\times10^{10}$.

A standing issue in turbulent thermal convection is the scaling of the large-scale velocity with the Rayleigh number Ra, $V \sim \mathrm{Ra}^{\gamma}$. As already mentioned briefly in Sec. I, various measurements using different techniques and different fluids in cells of different shape have yielded different values for the exponent γ ranging from 0.4 to 0.5, which may be divided into two groups [9]. The first one measures the LSC speed near the sidewall and most results [5,7,14,28,29] give $\gamma \approx 0.5$, which may be understood by thinking that flows there are driven by ballistic plumes with a free-fall type velocity. The second group measures the oscillation frequency of the LSC and most results [5,9,11,30–32] yield $\gamma \approx 0.42-0.47$, which may be understood by considering that the oscillation is associated with the rms velocity of the flow. Unlike previous results, the 0.4 result for our inner core is not arising from any oscillations but is associated with a spatially averaged velocity. Indeed, we did not see any oscillation in either the temperature or velocity fields in our cell. Since ω_o and ω_i are ''regional'' averages over areas occupied by the core and shell, our results suggest that different regional averages can give rise to different values of a scaling exponent for the large-scale velocity and that the scaling exponent alone is not sufficient to distinguish the various driving mechanisms for the flow. As far as we are aware, the only other work that measured the Ra scaling of the rotation frequency was that of Qiu and Tong, in which they found $\omega_o L^2/2\kappa = 1.1\mathrm{Ra}^{0.45}$ for the normalized rotation frequency in a cylindrical cell [4]. Since Ra in their experiment is less than 10^{10} and only one core is observed, we compare their result with our outer-shell and single core result. We note that the 0.5 exponent can be understood in terms of a free-fall type velocity or ballistically moving plumes. As we already pointed out there is no coherent temporal oscillations in our cell, which is present in cylindrical cells. This oscillation is presumably a horizontal wobbling of bulk fluid [9]. Because of this, viscous dissipation in the cylindrical cell should be larger than the rectangular one, which means more rigorous driving by the thermal plumes in the latter. This could explain why the exponent for the cylinder is smaller that the free-fall value.

B. Statistical quantities of velocity field

We now present some statistical quantities for $\mathrm{Ra} = 3.8\times10^9$ and 3.5×10^{10}, for which longer-time measurements at higher sampling rate have been made. Figure 9 shows the distribution of the root-mean-square (rms) velocity fluctuations color coded in unit of cm/s. The left panel shows the horizontal rms velocity u_{rms} and the right panel shows the vertical rms velocity w_{rms}, the top panel is for $\mathrm{Ra} = 3.8\times10^9$ and the bottom panel is for $\mathrm{Ra} = 3.5\times10^{10}$. If we note the scales of color bars, it is clear that the magnitude of vertical velocity fluctuation is much higher than that of the horizontal one, which becomes more so with increasing Ra. These large vertical fluctuations are caused by the intermittent emission of thermal plumes that rise and fall due to their buoyancy. Since the plumes are moving primarily along the sidewalls, velocity fluctuations are also concentrated in these regions. We also note that the regions of large w_{rms} correspond to where rising and falling plumes hit the opposite plates and create the counterrotating vortices, with increasing Ra these regions decrease in size but the fluctuations become more intense. For u_{rms}, it is seen that at lower Ra the regions of large horizontal velocity fluctuations are primarily confined near the top-left and lower-right corners, just like the vertical one. But at higher Ra, the regions of high u_{rms} have extended to the ''path'' of the mean wind, in contrast to the behavior of w_{rms}.

From Fig. 9 it is clear that ''cuts'' along the symmetry axes will miss the regions of the most intense velocity fluctuations. Nevertheless, it would still be interesting to compare such cuts with results from previous studies. Figure 10 shows the profiles of u_{rms} (solid circles) and w_{rms} (open squares) along the x axis (left panel) and z axis (right panel). In their cubic cell experiment, Tilgner, Belmonte and Libchaber also measured both u_{rms} and w_{rms} profiles as a function of z and found that both decay approximately linearly to a minimum at the cell center, after reaching their maximum

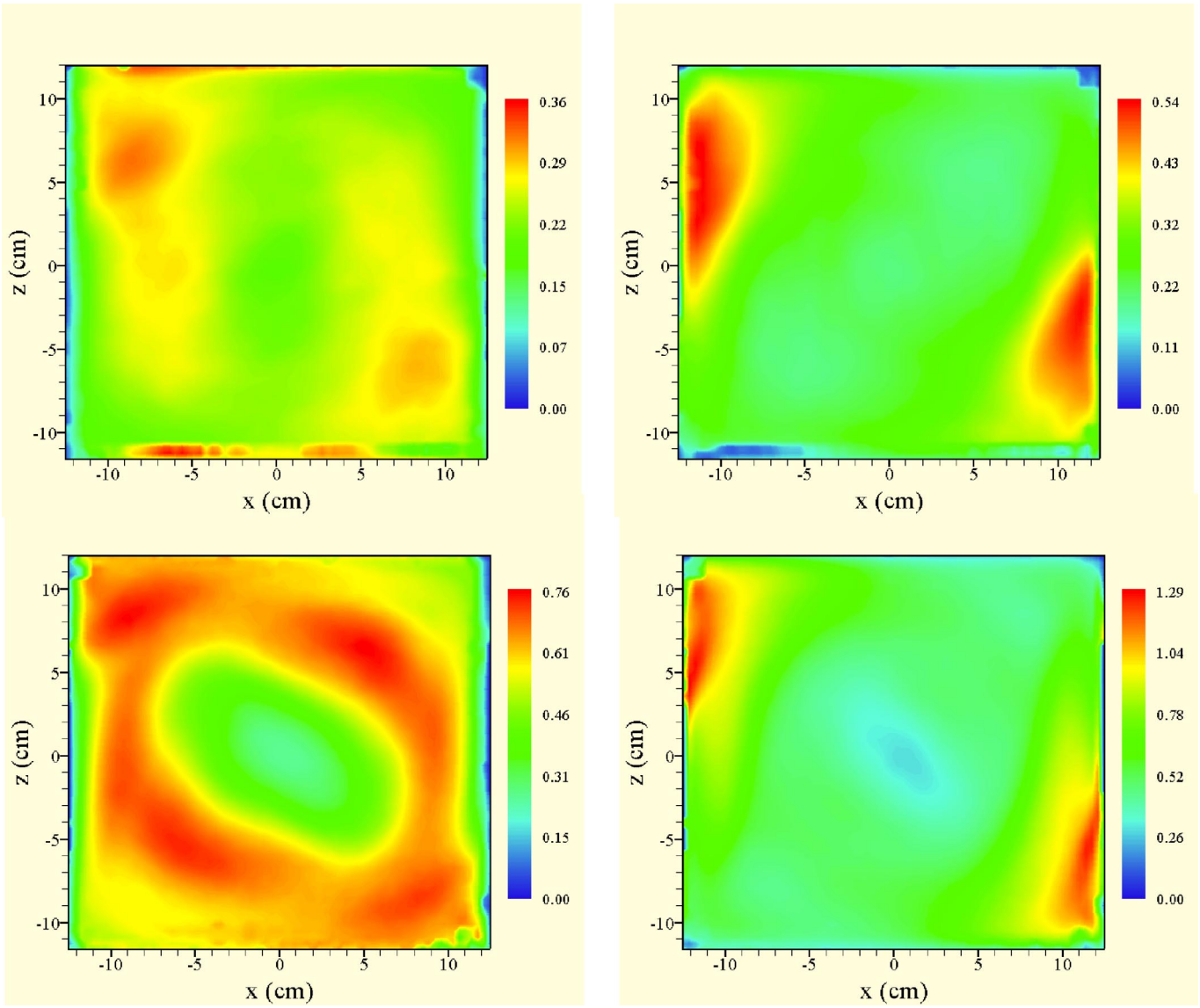

FIG. 9. (Color online) Contour map plots of the horizontal rms velocity u_{rms} (left panel) and vertical rms velocity w_{rms} (right panel) for Ra$=3.8\times10^{9}$ (upper panel) and 3.5×10^{10} (lower panel) in units of cm/s.

values near the boundary [26]. Another rms velocity profile measurement was done by Qiu and Tong in a cylindrical cell [4], also in water. What they found was that the rms profiles along the symmetry axes of the cell are more or less constant, except close to the cell boundary where the rms velocity has a peak. If we compare our rms profiles with these two experiments at a comparable value of Ra ($\approx10^{9}$), we see that the gross feature of our rms profiles is similar to that of Ref. [26] in that both have a local minimum at the cell center and the level of velocity fluctuations in the rectangular and cubic cells are smaller than those in the cylindrical cell for both the ''peak'' and ''bulk'' values (in the cylinder, the maximum rms values reach $5\sim6$ mm/s and remains 4 mm/s in the bulk). We think this lower level of velocity fluctuations in the rectangular cell may be related to the fact that there is no oscillation or wobbling in the horizontal plane as is the case in the cylindrical cell. On the other hand, the detailed features of our rms profiles and those from Ref. [26] are quite different. For example, the ''steps'' or plateaus in our case are absent for the cubic cell, which may be a reflection of the difference in cell geometry. At higher Ra our rms profiles also become more symmetric and less ''noisy'' and the ''valley'' at the cell center becomes more steep, indicating that flow in the cell center becomes relatively ''quieter'' as compared to flow in the cell's boundaries. This change of rms profiles with Ra is also consistent with what we have seen previously from the mean flow patterns, that the flow is better developed and more stable at higher Ra. Another feature to be noted is that u_{rms} and w_{rms} in the central region of the cell are neither constant nor of the same value (which is more obvious for the higher Ra); this implies that velocity fluctuations are neither homogeneous nor isotropic in this region. This feature can be seen more clearly in the skewness of the velocity field, which is shown in Fig. 11. The left panel of the figure shows the horizontal velocity skewness $S_u=\langle(u-U)^3\rangle/u_{rms}^3$ and the right panel shows the vertical

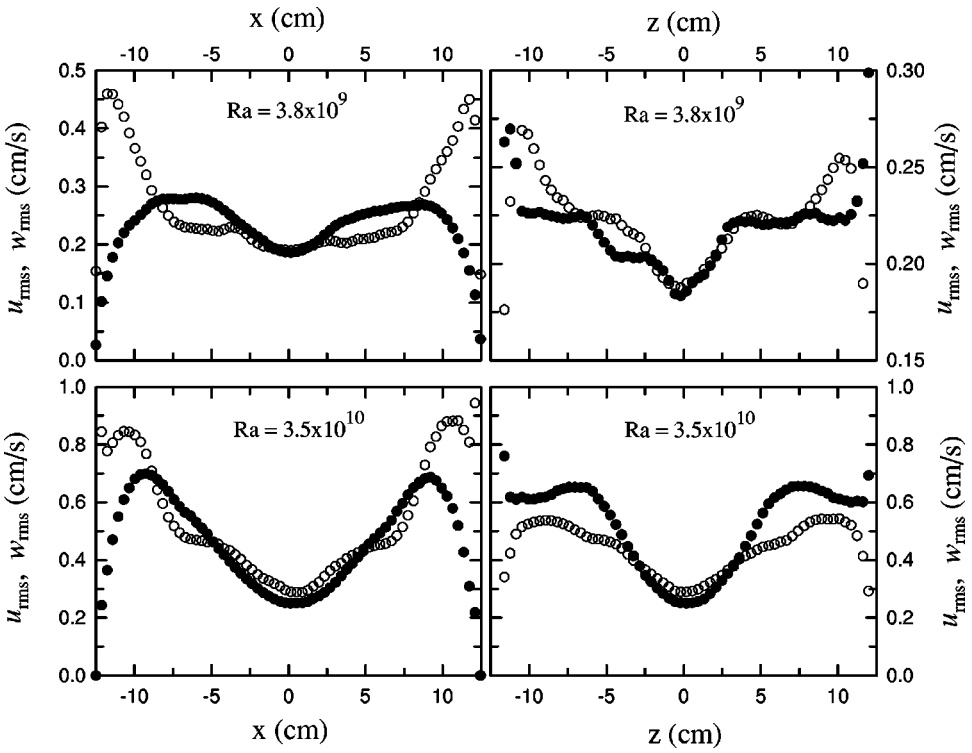

FIG. 10. Profiles of u_{rms} (dots) and w_{rms} (open circles) for the two values of Ra as indicated. Left panel: profiles cut along the x axis (at $z=0$). Right panel: profiles cut along the z axis (at $x=0$).

velocity skewness $S_w=\langle(w-W)^3\rangle/w_{rms}^3$; the top panel is for Ra$=3.8\times10^9$ and the bottom panel is for Ra$=3.5\times10^{10}$. The figure further shows that the flow field becomes more symmetric at higher values of Ra. We note that the regions of large skewness (the ''red'' and ''blue'' semicircles) correspond to the boundary between the inner core and the outer core.

To study the dynamics that drives the turbulent flow in the system, we examine the turbulent energy and Reynolds shear stress. Figure 12 shows the distribution of the turbulent kinetic energy per unit mass $k=\frac{1}{2}(u_{rms}^2+w_{rms}^2)$ (left panel) and the dominant component of the normalized Reynolds shear stress tensor $\langle u'w'\rangle/k$ (right panel) for the two Rayleigh numbers, where $u'(t)=u-U$ and $w'(t)=w-W$ are the fluctuating parts of u and w. Similar to the mean kinetic energy, the figure shows that with increasing Ra turbulent energy is increasingly concentrated near the two corners where ascending and descending plumes impinge the cold and hot boundary layers, respectively. The Reynolds stress τ_{ij} is responsible for the exchange momentum between turbulence and the mean flow and its existence requires the correlated fluctuations of u and w [33]. From Fig. 2 we see that the regions of large τ_{ij} correspond to where the hot and cold plumes start to accelerate along the sidewalls toward the opposite plates (see also Fig. 6); as coherent objects the different velocity components of a plume naturally have a high degree of correlation which results in large Reynolds stress. Since turbulence production is proportional to τ_{ij}, we see that the turbulent kinetic energy largely comes from the buoyant motions of thermal plumes. If we overlay the Reynolds stress map on the turbulent energy map and bear in mind that the flow is clockwise, we see that the regions of large τ_{ij} are upstream of the regions where turbulent energy (and dissipation) are concentrated, it shows how turbulent energy is extracted from the plumes via Reynolds stress and then dissipated, largely in the form of counter-rotating vortices near the opposite plate. When Krishnamurti and Howard first observed the existence of the large-scale flow, they suggested that the mean flow is driven by Reynolds stress associated with tilting plumes [1], which implies that the mean flow is maintained by turbulent fluctuations and thus a negative production. This assertion can be checked by examining the turbulent energy production $P(=-\langle u_iu_j\rangle\partial U_i/\partial x_j)$ [33] of the system. The production dictates energy transfer between the mean flow and turbulence, a negative production means the mean flow derives energy from turbulent fluctuations while a positive one implies that the mean flow supplies energy to the turbulent fluctuations, which is the typical situation for most flows. Figure 13 shows the color-coded production contour map for Ra$=3.5\times10^{10}$. It shows clearly that production is positive in most parts of the cell and is also overall positive when integrating over the whole two-dimensional plane. Thus, the mean flow is not driven by fluctuations or Reynolds stress associated with plumes. Rather, it is the buoyancy of the plumes that drive the mean flow as shown by Figs. 3 and 5.

C. Instant velocity field

Although the sampling rate of our measurements are rather low, the relatively slow fluctuations in thermal convection still allows us to obtain some useful information about the instant flow field. Here we examine some properties of the instantaneous velocity field, again for the two selected values of Ra which are measured at a higher sampling rate (3 Hz). Figure 14 shows the instantaneous 2D vector field with

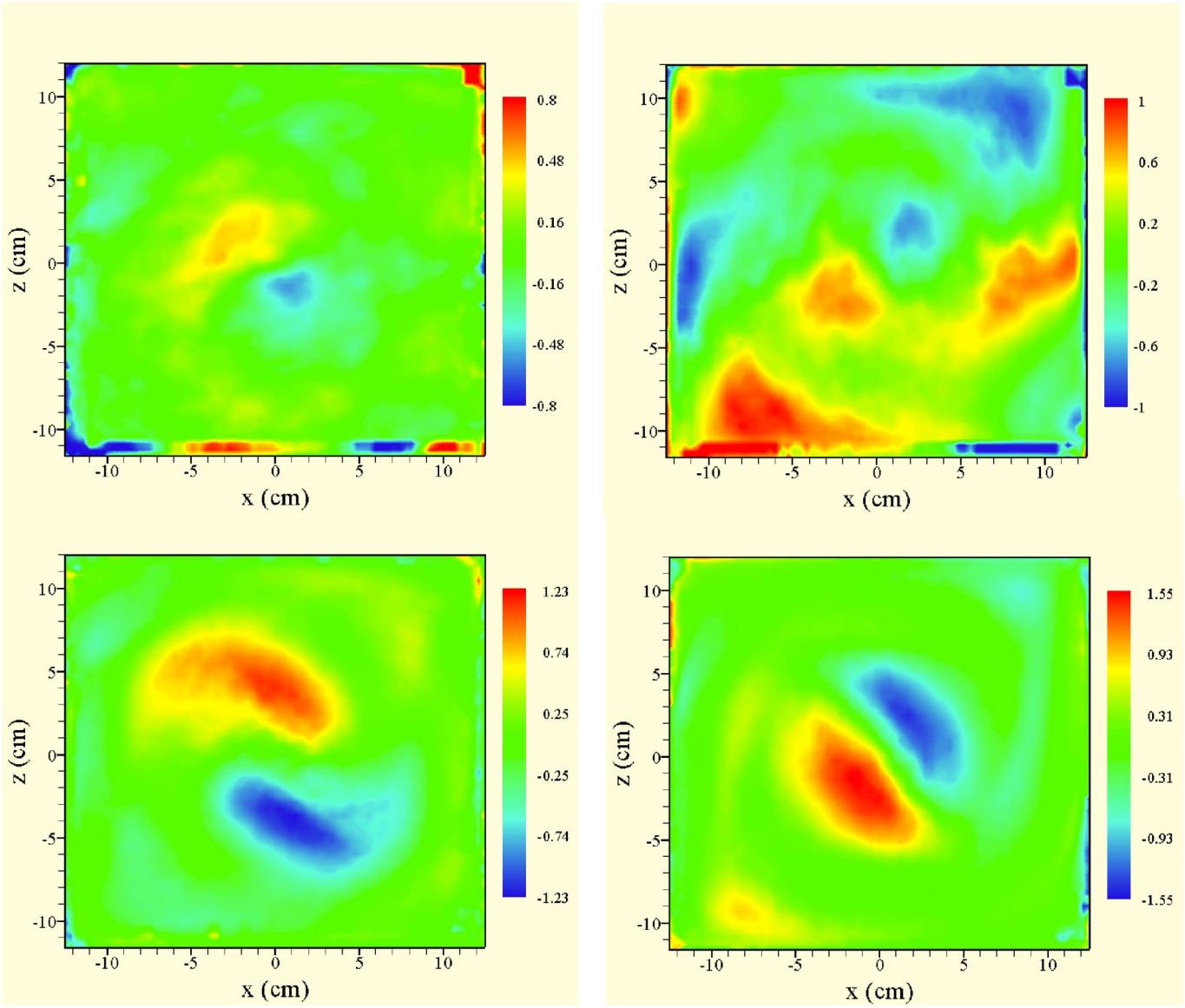

FIG. 11. (Color online) Contour map plots of the skewness for the horizontal velocity (left panel) and for the vertical velocity (right panel) for Ra$=3.8\times10^{9}$ (upper panel) and 3.5×10^{10} (lower panel).

the magnitude of the velocity $\sqrt{u(t)^2+w(t)^2}$ coded by color and by the length of the arrow for these two Ra. It is seen that the flow is highly turbulent around the periphery of the convection cell with 'bursts' like events (large velocity fluctuations) appearing in the upper-middle left wall and the lower-middle right wall, despite the fact that the mean velocity of the flow is rather low by the standard of nonthermal turbulence. By inspecting the velocity field measured at different instances, we also observed that bursts always occur in these regions [34]. Because of the high validation rate of our PIV measurement, we can see that many of the qualitative features exhibited by the long-time-averaged mean velocity maps (Fig. 2) can already be seen from a single measurement. These include (1) the overall flow is a clockwise global circulation, (2) there are two small vortices rotating counterclockwise at the upper left and lower right corners, (3) the flow becomes increasingly confined in regions near the sidewalls and the plates as Ra increases (i.e., the central low velocity region is growing), and (4) the roughly elliptical shaped ''quiet'' central region has different orientations for the two values of Ra.

In Figs. 15(a) and 15(b) we show the velocity time series over a period of $\sim$3,300 sec for two Rayleigh numbers taken at five positions in the small convection cell, one each close to the top and bottom plates and near the left and right sidewalls, and one at the cell center (the exact coordinates in unit of centimeters are indicated on the graph). Figure 15(a) shows the vertical velocity $w(t)$ near the sidewalls and at the cell center, for Ra$=3.8\times10^{9}$ (left panel) and Ra$=3.5\times10^{10}$ (right panel). Figure 15(b) shows the horizontal velocity $u(t)$ close to the plates and at the center for the same two values of Ra. We examine the vertical velocity first. Here we see that the ''mean'' flow is upward-going (defined as positive) and downward-going (defined as negative) near the left-sidewall and right-sidewall, respectively, which is of course consistent with the fact that the overall flow is clock-

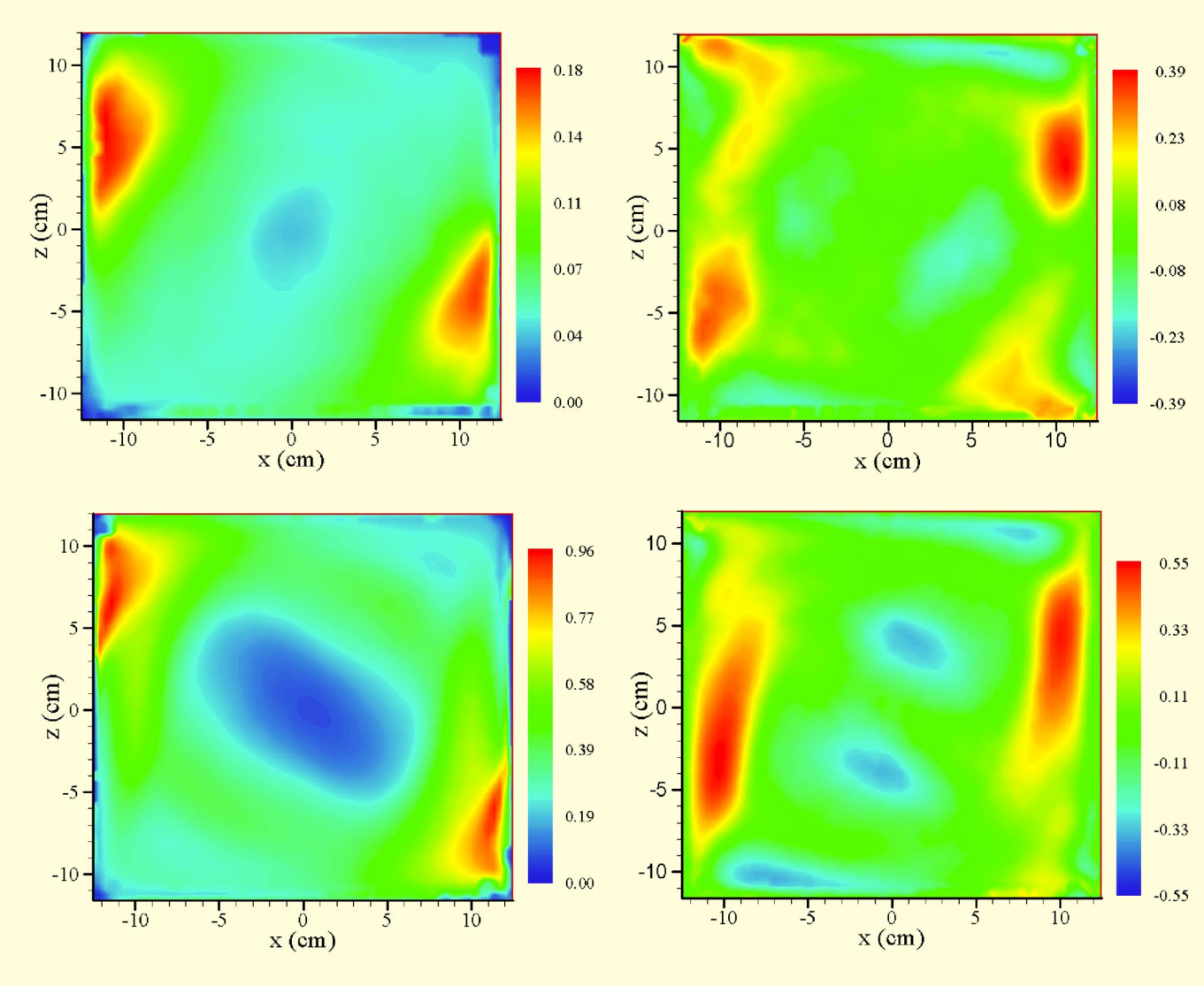

FIG. 12. (Color online) Turbulent kinetic energy (left panel) and normalized Reynolds shear stress (right panel) for $Ra=3.8\times10^9$ (upper) and 3.5×10^{10} (lower).

wise. At the cell center the velocity fluctuates in both directions with a zero mean. But a closer inspection shows that the flows near the sidewalls are different for the two Rayleigh numbers. For the lower Ra, we can clearly see that the velocity near the sidewalls shows occasional spikes of the opposite sign (those crossing the dashed lines), indicating that the local flow changes direction at that instant. It is well known that, in the steady-state flow in a convection cell, thermal plumes participate and drive the LSC in such a manner that hot plumes go up along one sidewall and cold plumes come down on the other [4,21]. The momentary directional reversal of local flow suggests that occasionally there are unusually energetic plumes going ''against the flow'' in their attempt to reach the opposite plate. This phenomenon has also been observed by Qiu *et al.* in a cylindrical cell of unity aspect ratio, in which the authors show that the velocity histogram near the sidewall has a clear bimodal distribution and they also attributed this to plumes going in the ''wrong'' route [35]. On the other hand, this feature is absent for the higher Ra. As can be seen from the mean flow maps (Fig. 3) at higher Ra the large-scale flow is more confined to the perimeter of the cell which means the associated plumes going in the ''right'' directions are reaching closer to the corners at the opposite plate before being mixed; this ''denies'' the opportunity for the ''opposite'' plumes going along the wrong sidewall. It should be noted that the above momentary reversal is not the same as the reversal of the mean wind observed mostly in cylindrical cells [8], as we do not see directional reversal for the overall flow. For example, no reversal is observed for $u(t)$ near the plates [Fig. 15(b)], despite the fact that these are simultaneous measurements. We believe the directional reversal of the wind is related to the bulk oscillation of the flow field and is perhaps unique to the particular shape of the cylindrical cell.

D. Velocity in the plane perpendicular to LSC

From the geometry of the cell, we expect the mean flow to be largely confined in the xz plane. Nevertheless, to obtain a

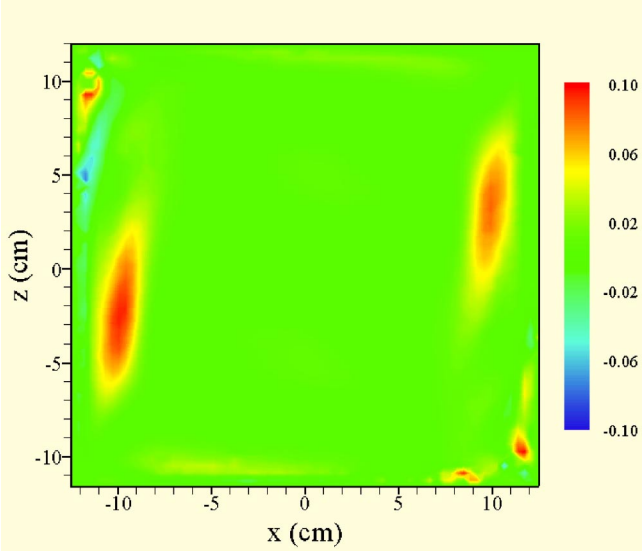

FIG. 13. (Color online) Contour map of the turbulent energy production P (in units of cm^2/s^3) for $Ra=3.5\times10^{10}$.

more complete picture on the flow field in the convection cell we made PIV measurements in the yz plane (at $x=0$) which is perpendicular to the mean wind, again for the two special values of Ra. Figure 16 shows the mean and the rms values of the velocity in this plane. Left panel: time-averaged velocity vector maps with the magnitude $\sqrt{V^2+W^2}$ coded in both color and the size of the arrow in unit cm/s. Middle and right panels: contour maps for v_{rms} and w_{rms}, respectively. The upper panel is for $Ra=3.8\times10^9$ and the lower one $Ra=3.5\times10^{10}$. For the lower Ra, the mean flow pattern shows that the y component of the velocity is essentially zero everywhere except the small vortices at the four corners, which confirms that the mean wind is confined mainly in the xz plane. Note that since the mean flow in the xz plane does not have a circular shape whereas the measurement is made at the middle vertical plane ($x=0$), this produces a relatively large vertical velocity near the middle of the top and bottom plate. The figure also shows that as the fluid hit the plates some will ''spill-over'' sideways to create the vortices at the corners. Note that the mean velocity at the top and bottom is not quite symmetric. We recall that the orientation of the elliptical core in the xz plane for this Ra is not along the diagonal direction but is at an $\sim20°$ angle with the horizontal, which means a cut at the middle vertical plane ($x=0$) will not produce a symmetric result. Indeed for the higher Ra, the mean flow becomes more symmetric as the elliptical core is now oriented along the diagonal of the cell. An important feature revealed by the figure is that the plane of the large-scale mean flow at higher Ra becomes aligned along the diagonal plane of the cell (i.e., along the diagonal from the upper-left corner to the lower-right corner in Fig. 16) and thus makes an angle with the xz plane, not parallel to it as is the case for lower Ra. This can be seen from the fact that there are now only two vortices at the top-right and lower-left corners. This is because the main flow is now against the sidewall plates at the top-left and lower-right corners and there is no room for the fluid to spill-over to the other direction to create vortices at these two corners. This tilting of the rotational plane of the mean wind at higher values of Ra suggests that the flow likes to assume a configuration having the largest spatial extend allowed by the geometry of the convection cell, as it corresponds to the most stable mode.

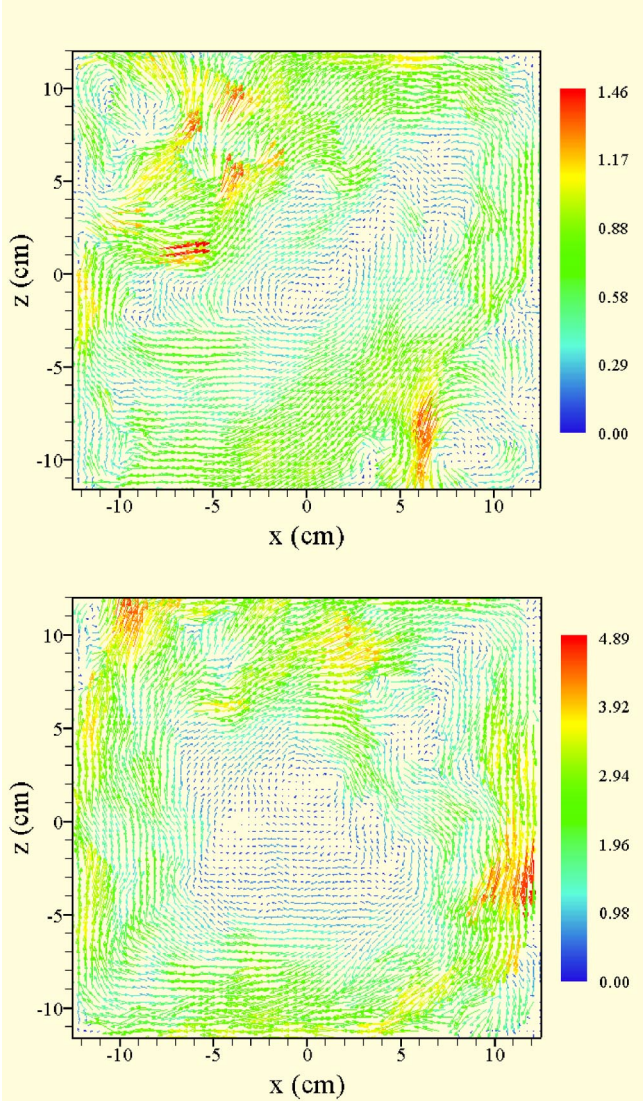

FIG. 14. (Color online) Snapshots of the velocity field viewed from the front, (a) $Ra=3.8\times10^9$ and (b) $Ra=3.5\times10^{10}$. The velocity magnitude is coded by both the length of the arrows and color in cm/s.

The maps for the rms velocities show that most of the fluctuations and dissipations are associated with the vortices at the corners. But at lower Ra, these fluctuations (and the corresponding turbulent kinetic energies) are dominated by the vertical component (w_{rms}) which is probably a reflection of the fact that the vortices at lower Ra are stretched along the vertical direction and thus have a smaller horizontal size. Whereas at higher Ra horizontal fluctuations become comparable to the vertical one, the latter is still slightly more concentrated and intense. The rms maps also show that although the mean velocity along the y direction is zero in the central part of the cell, the corresponding fluctuations (v_{rms}) are rather significant.

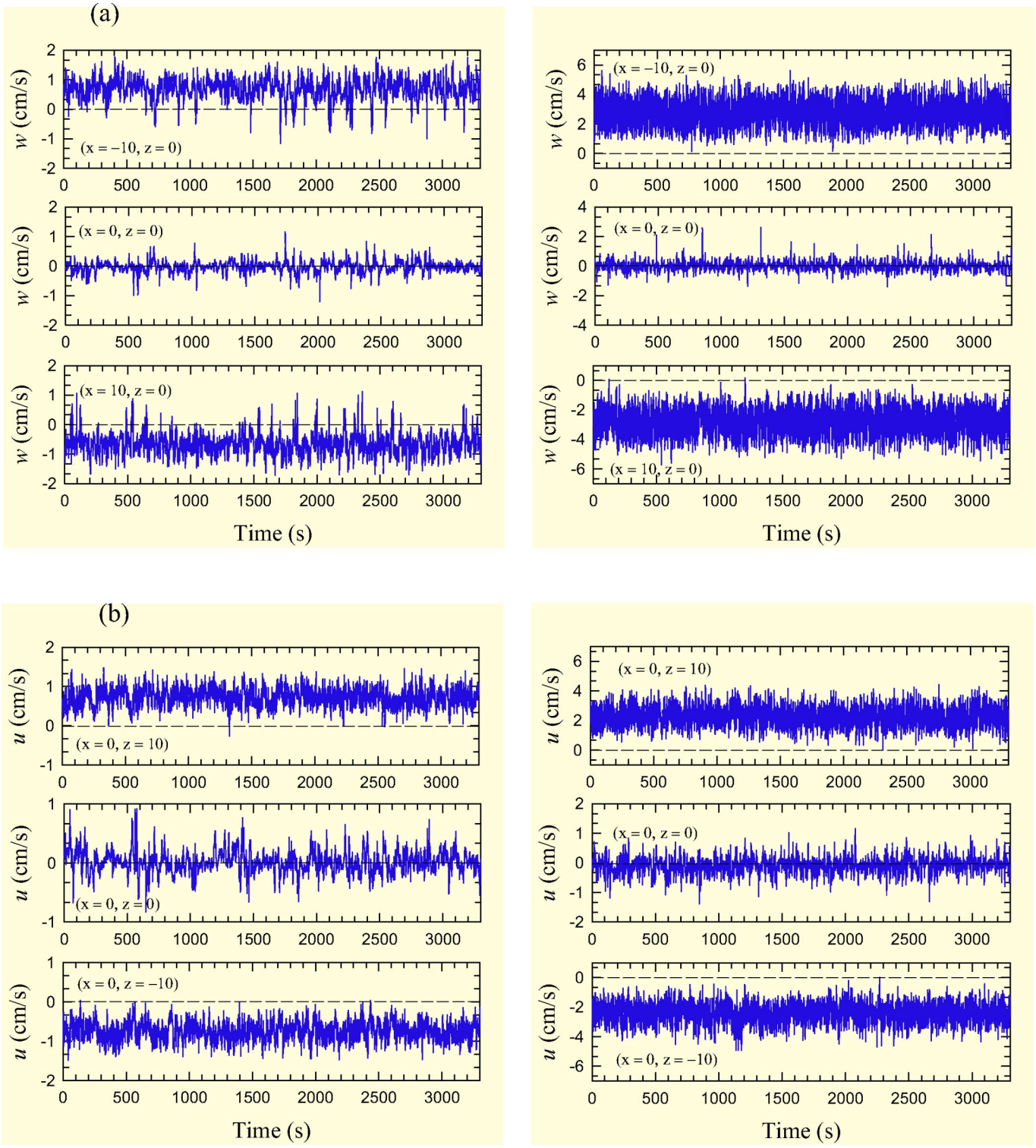

FIG. 15. (Color online) (a) Time series of the vertical velocity at three positions in the small convection cell, from top to bottom: near left sidewall, at cell center, and near right sidewall (the exact coordinates of the positions are indicated on the figure in units of cm). (b) Time series of the horizontal velocity at three positions, from top to bottom: below the top plate, at cell center, and above the bottom plate. In both (a) and (b), the left panel is for $\mathrm{Ra}=3.8\times10^{9}$ and the right panel for $\mathrm{Ra}=3.5\times10^{10}$.

IV. SUMMARY AND CONCLUSION

In the work reported in this paper we have made a systematic investigation of the properties of the velocity field in two Rayleigh-Bénard convection cells of same geometry, with the Rayleigh number Ra varying from 9×10^{8} to 9×10^{11} while the Prandtl number remained approximately constant (~4). Time-averaged 2D velocity fields are measured in both the plane of the large-scale mean flow (the

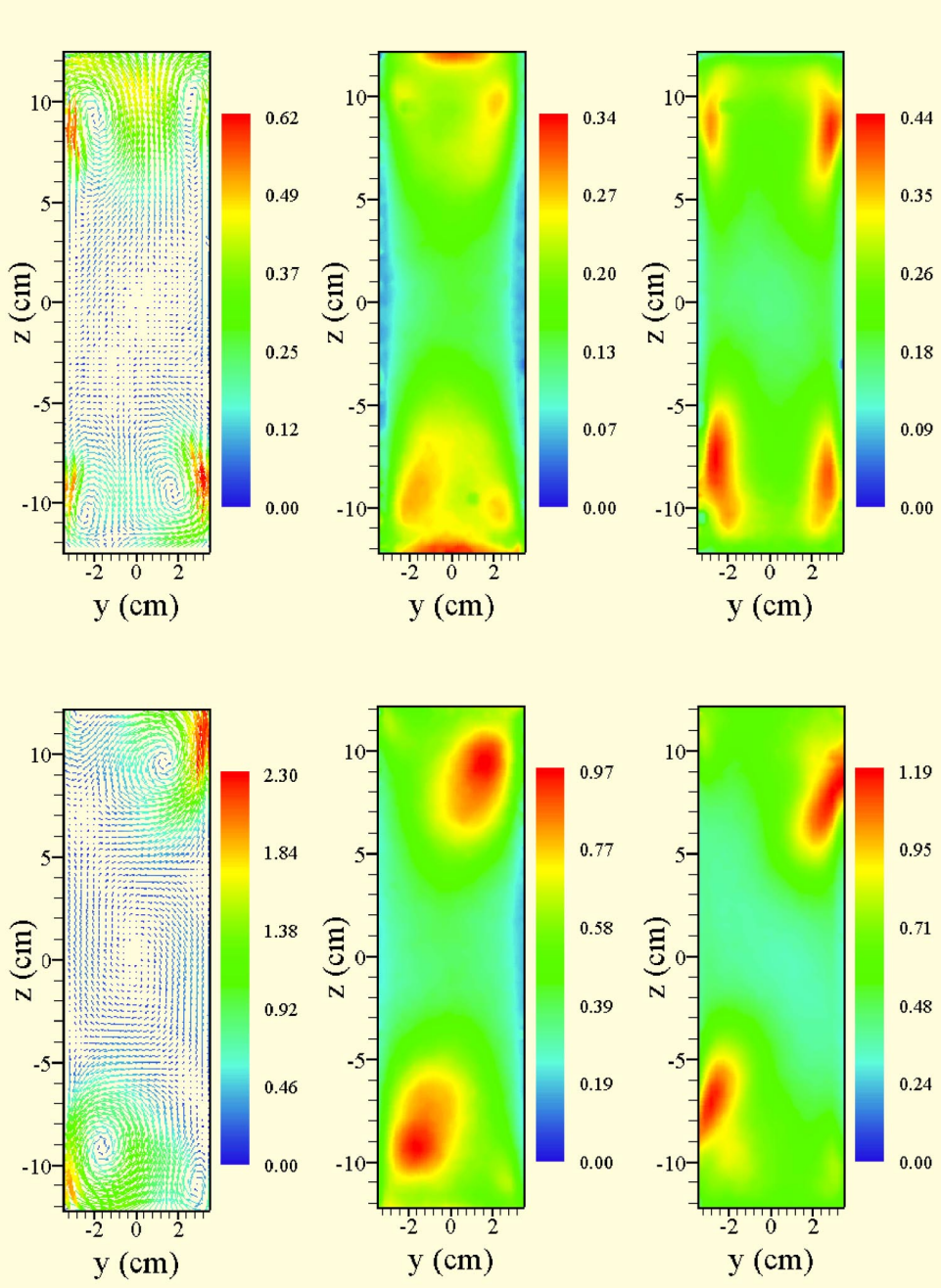

FIG. 16. (Color online) Mean and rms values of velocity in the plane perpendicular to the mean wind. Left panel: Time-averaged velocity field with the magnitude $\sqrt{U^2+W^2}$ coded in both color and the size of the arrow in units of cm/s. Middle and right panels: Contour maps for v_{rms} and w_{rms}, respectively. The upper panel is for Ra$=3.8\times10^9$ and the lower one for Ra$=3.5\times10^{10}$.

wind) and that perpendicular to the wind, using the particle image velocimetry (PIV) technique over the range of Ra spanned in the experiment (three decades). For two selected values of Ra, certain statistical and dynamical quantities of the velocity field are also obtained. The measurement provides a direct confirmation that a rotatory mean wind indeed persists for the value of Ra close to 10^{12}, at least in water or in systems with comparable values of the Prandtl number.

From the measured two-dimensional velocity field in the plane of the mean wind, four prominent features or regions of the flow field are identified: (1) A central low-velocity rotatory core; (2) two low-velocity or stagnation regions at the lower-left and upper-right corners; (3) two high-velocity regions, one stretches from the eight-o'clock position to the one-o'clock position and the other from the two-o'clock position to the seven-o'clock position in the box; and (4) two counter-rotating vortices at the upper-left and lower-right corners.

By studying the Ra-dependent properties, we find the following: (1) An inner rotational core is formed inside a bulk outer rotational shell when Ra becomes larger than 1×10^{10}, below this Ra only one core is observed. Comparing the instant vector map and the time-average ones, we see that the flow field can exhibit coherent structures at different length scales depending on the time scale we look at them. (2) The rotational frequency of the outer-shell may be taken as the average rotation rate of the mean wind and it has an exponent of 0.5 for the Ra scaling, whereas the inner core has a distinctly different scaling with an exponent of 0.4. The results suggest that different regional averages can give rise

to different values of scaling exponent for the large-scale velocity and that scaling exponent alone is not sufficient to distinguish the various driving mechanisms for the flow. It also partly explains why there are varying values for this exponent from different experiments. (3) With increasing Ra, the mean wind becomes increasingly confined near the perimeter of the convection cell, and a similar trend is also found for both the mean flow kinetic energy and turbulent kinetic energy.

The measurements made for two selected values of Ra, at higher sampling frequency and also in the plane perpendicular to the mean wind, reveal the following properties: (1) The rms and skewness maps of the velocity field show that the velocity fluctuations at the cell center are neither homogenous nor isotropic, the skewness maps further show that there are large asymmetric velocity fluctuations at the core-shell boundary. (2) The measured Reynolds shear stress distributions indicate that the turbulent production is largely positive, which implies that the large-scale mean flow is not driven by turbulent fluctuations. (3) Velocity measurement in the plane perpendicular to the mean wind reveals that the flow likes to be in a configuration with the largest spatial extent allowed by the geometry of the convection cell, which corresponds to the most stable mode. In this particular case, it means that even with the small aspect ratio in the yz plane, the rotational plane of the mean wind is aligned along the diagonal of the convection box.

If we combine results from the present experiment and from some of the previous studies by others, the following picture emerges: thermal plumes are first accelerated along the sidewalls, reach maximum velocity, then impinge on the plates, thereby creating counter-rotating vortices near the corners where turbulent energy (and dissipation) is concentrated. Furthermore, the thermal plumes not only drive the mean flow via their buoyancy but also provide energy for turbulent fluctuations via the associated Reynolds stress. The emergence of the inner core inside a bulk rotating core is a striking example of how complex systems are capable of self-organizing into coherent structures. Because heat is transported mainly along the periphery of the cell by thermal plumes [25], it is not sensitive to changes in the cell interior. This is why the transition in the flow state was not detected in previous measurements of global quantities like heat flux or in velocity measurements near sidewalls.

To understand the origin for the discovered core-shell structure and why it has such a sharp boundary with a large mismatch in shear stress poses a new theoretical challenge and also calls for more systematic experimental investigations. It will be of interest to know what will become of the core-shell structure at yet even higher values of Ra, or if the current flow state already is the asymptotic one. Understanding this structure and the associated transition will undoubtedly enrich our knowledge not only about turbulent convection but also many natural phenomena.

ACKNOWLEDGMENTS

We have benefited from stimulating and helpful discussions with many people, in particular P. Tong, L.P. Kadanoff, A. Thess, F. Busse, R. Ecke, and K.R. Sreenivasan. This work was supported by the Research Grants Council of Hong Kong SAR under Project No. CUHK4224/99P and by CUHK Research Committee under Project No. 2060229.

[1] R. Krishnamurti and L. N. Howard, Proc. Natl. Acad. Sci. U.S.A. **78**, 1981 (1981).
[2] S. Grossmann and D. Lohse, J. Fluid Mech. **407**, 27 (2000).
[3] X. Chavanne, F. Chillà, B. Chabaud, B. Castaing, and B. Hébral, Phys. Fluids **13**, 1300 (2001).
[4] X.-L. Qiu and P. Tong, Phys. Rev. E **64**, 036304 (2001).
[5] J.J. Niemela, L. Skrbek, K.R. Sreenivasan, and R.J. Donnelly, J. Fluid Mech. **449**, 169 (2001).
[6] G. Zocchi, E. Moses, and A. Libchaber, Physica A **166**, 387 (1990).
[7] M. Sano, X.-Z. Wu, and A. Libchaber, Phys. Rev. A **40**, 6421 (1989).
[8] K. R. Sreenivasan, A. Bershadskii, and J. J Niemela, Phys. Rev. E **65**, 056306 (2002).
[9] X.-L. Qiu and P. Tong, Phys. Rev. E **66**, 026308 (2002).
[10] S. Grossmann and D. Lohse, Phys. Rev. E **66**, 016305 (2002).
[11] S. Lam, X.-D. Shang, S.-Q. Zhou, and K.-Q. Xia, Phys. Rev. E **65**, 066306 (2002).
[12] See, for example, M. Raffel, C. Willert, and J. Kompenhans, *Particle Image Velocimetry* (Springer Press, Berlin, 2000).
[13] X.-L. Qiu, S.-H. Yao, and P. Tong, Phys. Rev. E **61**, R6075 (2000).
[14] X.-L. Qiu and K.-Q. Xia, Phys. Rev. E **58**, 486 (1998).
[15] J.-J. Wang and K.-Q. Xia, Eur. Phys. J. B **32**, 127 (2003).
[16] J.A. Glazier, T. Segawa, A. Naert, and M. Sano, Nature (London) **398**, 307 (1999).
[17] We also used 4 μm diameter polystyrene spheres in some of the earlier measurements and essentially the same results are obtained as far as mean velocity is concerned.
[18] R.J. Adrian, Annu. Rev. Fluid Mech. **23**, 261 (1991).
[19] These measurements were made in the early stage of the experiment where 4 μm diameter spheres were used. Later on 50 μm particles were used in the measurements in small cells. These two types of particles produced essentially the same result for the mean velocity. The difference is that the larger particles have a stronger light scattering intensity and thus the effect of wall reflections becomes less of a problem. The large particles also produce a higher validation rate for the velocity vectors because their image on the CCD sensor is comparable to the size of a pixel, thus for the same amount of averages they produce better statistics.
[20] These counter-rotating vortices can also be seen from the coarse-grained vector map Fig. 2 and instant velocity field Fig. 13, and also from animated movies (see Ref. [34]).
[21] L.P. Kadanoff, Phys. Today **54**(8), 34 (2001).
[22] J.J. Niemela, L. Skrbek, and K.R. Sreenivasan, Europhys. Lett. **62**, 829 (2003).
[23] X.-L. Qiu and P. Tong, Phys. Rev. Lett. **87**, 094501 (2001).
[24] E. Villermaux, Phys. Rev. Lett. **75**, 4618 (1995).

[25] X.-D. Shang, X.-L. Qiu, P. Tong, and K.-Q. Xia, Phys. Rev. Lett. **90**, 074501 (2003).
[26] A. Tilgner, A. Belmonte, and A Libchaber, Phys. Rev. E **47**, R2253 (1993).
[27] S.-Q. Zhou, Ph.D. thesis, The Chinese University of Hong Kong, 2002.
[28] T. Takeshita, T. Segawa, J. A. Glazier, and M. Sano, Phys. Rev. Lett. **76**, 1465 (1996).
[29] X. Chavanne, F. Chillà, B. Castaing, B. Hébral, B. Chabaud, and J. Chaussy, Phys. Rev. Lett. **79**, 3648 (1997).
[30] B. Castaing *et al.*, J. Fluid Mech. **204**, 1 (1989).
[31] S. Cioni, S. Ciliberto, and J. Sommeria, J. Fluid Mech. **335**, 111 (1997).
[32] S. Ashkenazi and V. Steinberg, Phys. Rev. Lett. **83**, 3641 (1999).
[33] See, for example, H. Tennekes and J. L. Lumly, *A First Course in Turbulence* (MIT Press, Cambridge, MA, 1972).
[34] See EPAPs Document No. E-PLEEE8-68-032312 for animated movies showing fluid flow in the 2D plane. A direct link to this document may be found in the online article's NTML reference section. The document may also be reached via the EPAPS homepage (http://www.aip.org/pubservs/epaps.html) or from ftp.aip.org in the directory /epaps/. See the EPAPS homepage for more information. These movies can also be viewed at www.phy.cuhk.edu.hk/turbulence/movies/. The movies are made by concatenating the consecutivley measured instant velocity fields.
[35] X.-L. Qiu, X.-D. Shang, P. Tong, and K.-Q. Xia, Phys. Fluid (to be published).